JOURNAL OF SOLID STATE CHEMISTRY 29, 165–179 (1979)

On the Structure of the Intermediate Phases in the Praseodymium Oxide System*

R. T. TUENGE AND LEROY EYRING**

Department of Chemistry and the Center for Solid State Science, Arizona State University, Tempe, Arizona 85281

Received September 28, 1978

The defect crystal structures for two phases in the praseodymium oxide system (Pr_9O_{16}, ζ phase; and $Pr_{40}O_{72}$, ε phase) are proposed on the basis of the the results of a high-resolution transmission electron microscope (HRTEM) study. Dynamical n-beam electron scattering calculations are used to provide a more accurate and reliable interpretation of the experimental micrographs. In addition, electron diffraction studies reveal the unit-cell dimensions for the $n = 11$ member in the homologous series of phases in this system. The structural relationships among the related praseodymium oxide phases are discussed.

Introduction

High-resolution transmission electron microscopy (HRTEM) has proved to be a powerful technique for the characterization of defects, especially extended defects, in solids. Recently, this technique has been applied to the praseodymium oxides, which display a homologous series of intermediate phases with formula Pr_nO_{2n-2} ($n = 7, 9, 10, 11, 12$) based on ordering of the oxygen vacancies in the oxygen-deficient fluorite structure. The results have been encouraging despite the fact that the fluorite superstructures are not ideally suited to crystal structure imaging for a variety of reasons. They do not, for example, exhibit large potential variations on a scale comparable to the resolution limit of an electron microscope. Furthermore, the shortest projection axis, the a-axis of the superstructures, is still relatively long (6.7 Å) for the approximations used in the image calculations. Lamentably, for this study, some of the fluorite superstructures readily decompose when exposed to the high electron beam radiation of the microscope.

Skarnulis *et al.* (*1*), however, have shown that HRTEM images of the ordered phase Pr_7O_{12}, the structural prototype of the homologous series, correlate with images calculated from the refined atom positions (*2*) in this rhombohedral superstructure if specimen and microscope conditions are well defined. When viewed down the $[100]_7$ direction the oxygen vacancies in ι phase are exposed as pairs (one pair/cell) having a separation of 3.7 Å in projection, a distance comparable with the point resolution of the HRTEM.

The encouraging results of the image contrast comparison for a known structure in the rare earth oxides have suggested the

* This work was supported by the National Science Foundation under Grant DMR 77-08473.

** To whom inquiries should be made.

0022-4596/79/080165-15$02.00/0

application of this method for the investigation of the defect structure of all of the phases in these systems. Various models for the oxygen vacancy arrangement can be tested by comparing the contrast of the high-resolution electron micrographs with that calculated from the structural model using dynamical scattering theory. This method has most recently been applied to the even-membered homolog $Pr_{24}O_{44}$ (β phase, $n = 12$) (*3*). The structural model proposed for this intermediate phase has oxygen vacancies occurring as pairs across alternating segments of (135) and ($1\bar{5}\bar{3}$) fluorite planes separated by 12 such planar spacings based on the agreement of calculated and observed crystal structure images. This proposed structure for β phase is an extension of the structural principle proposed by Kunzmann and Eyring (*4*) for odd-members of the R_nO_{2n-2} series of phases in the praseodymium and terbium oxide systems.

Refined crystal structures of the other ordered intermediate phases in the praseodymium oxide system have not been obtained, so far. This is true in spite of the effort to obtain satisfactory data sets from X-ray diffraction from single crystals of both ζ and ε phases and total-profile neutron diffraction data from powders of these two phases (*5*). The most likely cause is an unpredictable twinning in the single crystal where the absorption correction for X-rays is very large and, in these circumstances, impossible to calculate accurately. In the case of neutron diffraction from powders the number of parameters to be determined was too large for the quality of the data and the resolution of the instrument. The purpose of the work described here, therefore, is to investigate via high-resolution crystal structure imaging the structure of the remaining intermediate phases in the praseodymium oxide system—ζ phase (Pr_9O_{16}), ε phase ($Pr_{40}O_{72}$, $n = 10$), and a polymorph of δ phase ($Pr_{88}O_{160}$, $n = 11$).

Experimental Procedure

Specimen Preparation

Single crystals of PrO_2 generally between 0.1 and 0.5 mm in each dimension were prepared by the hydrothermal method described by Lowenstein *et al.* (*6*). The oxygen content was adjusted to those values corresponding to the intermediate phases in the series Pr_nO_{2n-2} with $n = 9$, 10, and 11 by treatment of the crystals on a Cahn microbalance under the following conditions: $PrO_{1.778}$ was annealed at 507°C and 10 Torr oxygen pressure for 7 days, then cooled to room temperature while the oxygen pressure was adjusted in order to maintain constant composition. $PrO_{1.80}$ was annealed at 450°C and 10 Torr oxygen pressure for 10 days and subsequently cooled to room temperature at constant weight. Cooling was accomplished in these two cases in 5 min. $PrO_{1.818}$ was annealed at 450°C and 10 Torr oxygen pressure for 5 days, then cooled for 8 min. to room temperature without maintaining constant weight. Laue and precession X-ray diffraction techniques and a Syntex $P\bar{1}$ autodiffractometer were used to investigate crystals of Pr_9O_{16} and $Pr_{10}O_{18}$ (*5*).

Electron Microscope Examination

In preparation for examination the crystals were ground in an agate mortar containing liquid nitrogen. The fragments were mounted on a holey carbon support film and examined with a modified JEM-100B transmission electron microscope. Electron diffraction patterns and images were obtained from thin parts of the fragments which projected over the support film after alignment with desired crystal zones as described by Iijima (*7*).

Calculations

Crystal structure image contrast was calculated taking into account the dynamical scattering of electrons using the n-beam multislice method described by Allpress *et al.*

(*8*) and O'Keefe (*9*), derived originally by Cowley and Moodie (*10*). The computer program FCOEFF (*1*) was used to calculate the structure factors of each reflection using the atomic scattering factors for electrons obtained from the International Tables (*11*). The electrostatic potential projected in a particular crystal direction and the dynamical scattering amplitude of each reflection at various thicknesses were calculated using a modification of the program DEFRACT, which is itself a modification of DEFECT (*1*), to include the effect of partial coherence of the objective aperture illumination. The image resulting after scattering through any number of slice thicknesses was calculated and displayed using the program IMAGER, a modification of the routine DISPLAY (*1*), which uses either an overprinting routine on a line printer or a halftone method on a graphics terminal.

Results and Discussion

ζ Phase—Pr_9O_{16}

The unit cell for the ζ phase of Pr_9O_{16} has been determined by electron diffraction (*4*) as triclinic, having the fluorite axial relationships:

$$a = a_F + \tfrac{1}{2}b_F - \tfrac{1}{2}c_F$$
$$b = \tfrac{3}{2}b_F + \tfrac{1}{2}c_F,$$
$$c = \tfrac{1}{2}a_F - \tfrac{1}{2}b_F + c_F.$$

On the basis of the similarity of the ζ-phase and ι-phase unit cells (ζ has two $\frac{1}{2}[211]_F$ axes in common with ι), Kunzmann and Eyring proposed that the arrangement of oxygen vacancies along these axes could be the same in both phases. This model would thus produce vacancy doublets parallel to the *a*–*c* plane stacked in the *b*-direction and separated by the *b*-axis length. There is, however, an array of oxygen vacancies almost identical to the proposed structure in which the vacancy pairs along the $\langle 21\bar{1}\rangle_F$ axis are inclined at 84.4° to the $(135)_F$ plane instead of at 73·0° as in ι. In this alternate structural model the 6-coordinated cations occur in strings in the $[111]_F$ direction, as they do in the ι phase. The two models for the structure of ζ are shown projected in both the [100] and [001] directions in Fig. 1 (*12*).

Numerous crystals of ζ phase were examined by single-crystal X-ray diffraction. Crystals obtained from different preparations often contained multiple orientations. those that were single displayed rather diffuse spots for both sublattice and superlattice reflections as observed on Laue photographs, indicating that these crystals were substantially disordered (*5*).

Figure 2 shows an experimental $[100]_9$ orientation electron diffraction pattern of a crystalline fragment of ζ phase. The reflections are indexed and the position of the 40-μm objective aperture used for imaging is indicated. The scattering amplitude of each reflection out to the 12th order was calculated dynamically by the multislice method for both vacancy models. The interaction of 585 beams was included in the calculation. The slice thickness was the *a*- and *c*-axis lengths (6.5 Å) for both the $[100]_9$ and $[001]_9$ direction projections. The amplitude and phase obtained for the central beam, a sublattice reflection, and a superlattice reflection are represented as a function of thickness up to 312 Å in Figs. 3a and b for the vacancy model shown in Fig. 1a. The amplitude of the 000 beam initially decreases with increasing thickness, reaching the first minimum point at a value of 65 Å, where the first equal-thickness contour will appear in the image. The 000 beam and the intense $0\bar{1}2$ sublattice reflection roughly form a two-beam case resulting in periodic scattering intensity up to at least 300 Å. The computed images are often more sensitive to the diffracted beam phases than to their amplitudes. Figure 3b shows that the phase difference between the central beam and the diffracted beams is approximately the same

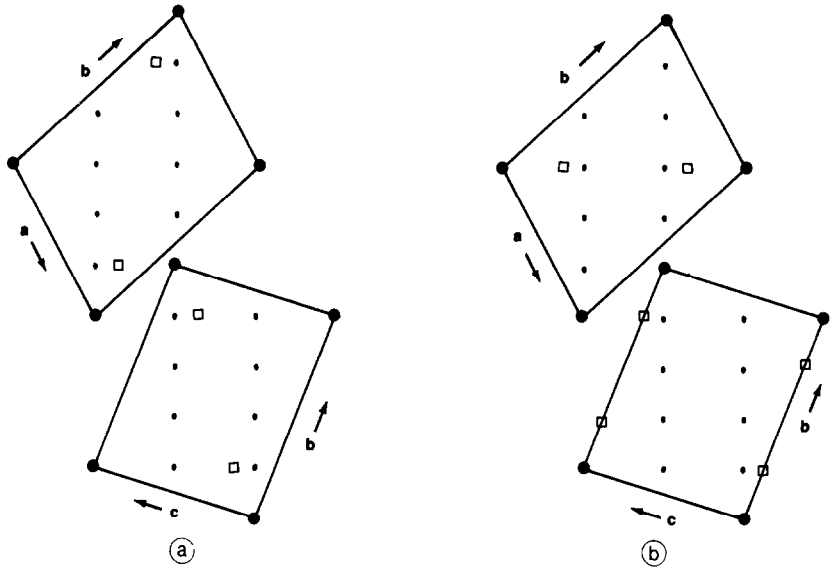

FIG. 1. The possible structures of ζ phase (Pr_9O_{16}) projected down both the [100] and [001] directions. ●, 6-coordinate cation; □, anion vacancy; •, cation.

as at zero thickness and relatively constant in the thickness intervals 0–50, 130–170, and 240–280 Å, where good structure images should be obtained.

Images were computed for the structural models of ζ phase over the range of crystal thickness, taking into account defocusing conditions. The experimental parameters of the electron microscope used in the calculation were: spherical aberration constant, $C_S = 1.8$ Å; half-width of depth of focus, Gaussian, $\Delta = 120$ Å; and beam divergence

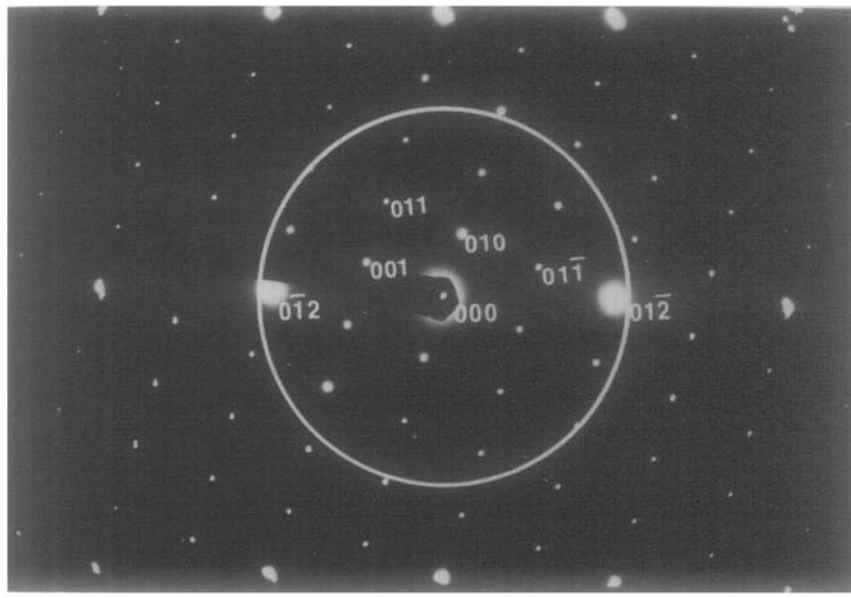

FIG 2. An experimental electron diffraction pattern of ζ phase in the $[100]_9$ orientation.

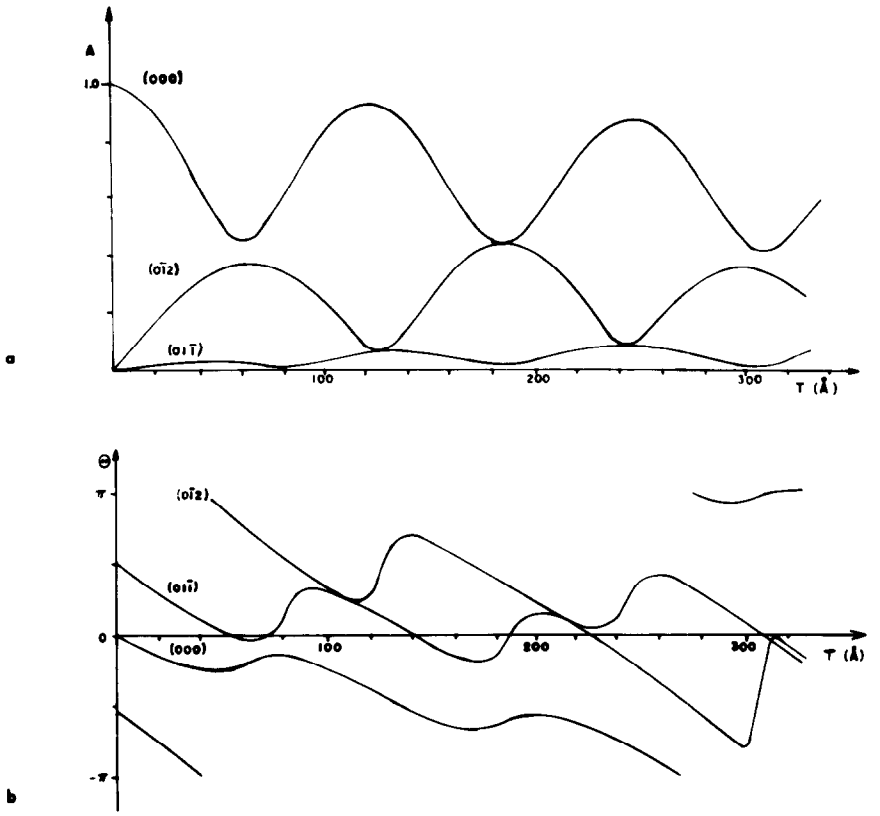

FIG. 3. (a) The amplitude and (b) the phase for the central beam, a sublattice reflection, and a superlattice reflection.

angle, $\theta_c = 0.9$ mrad. Figures 4a and b show a series of $[100]_9$ and $[001]_9$ projection images, respectively, calculated for the vacancy model of ζ with oxygen vacancy pairs inclined at 73° to the $(135)_F$ planes (Fig. 1a). The atomic positions used for this model are listed in Table I. The metal positions were obtained by comparison with refined positions in ι phase (Pr_7O_{12}), and the oxygen positions were not altered from their ideal fluorite sites. It is evident by comparison with the projected structure that for thin crystals (up to 52 Å) at −900 Å defocus, rows of oxygen vacancies aligned parallel to the electron beam are imaged as white spots, while those of occupied oxygen and praseodymium are included in the dark area and are not distinguished. The calculations

TABLE I

ATOMIC POSITIONS FOR THE PROPOSED STRUCTURE OF ζ PHASE (Pr_9O_{16}) SYMMETRY $P\bar{1}$

Atom No.	x	y	z
Pr1	0.000	0.000	0.000
Pr2	0.238	0.109	0.586
Pr3	0.468	0.234	0.107
Pr4	0.873	0.468	0.234
Pr5	0.667	0.333	0.667
Oxygen vacancy	0.139	0.194	0.222
O2	0.250	0.750	0.000
O3	0.306	0.028	0.889
O4	0.472	0.861	0.555
O5	0.639	0.694	0.222
O6	0.806	0.528	0.889
O7	0.972	0.361	0.555
O8	0.083	0.917	0.333
O9	0.417	0.583	0.667

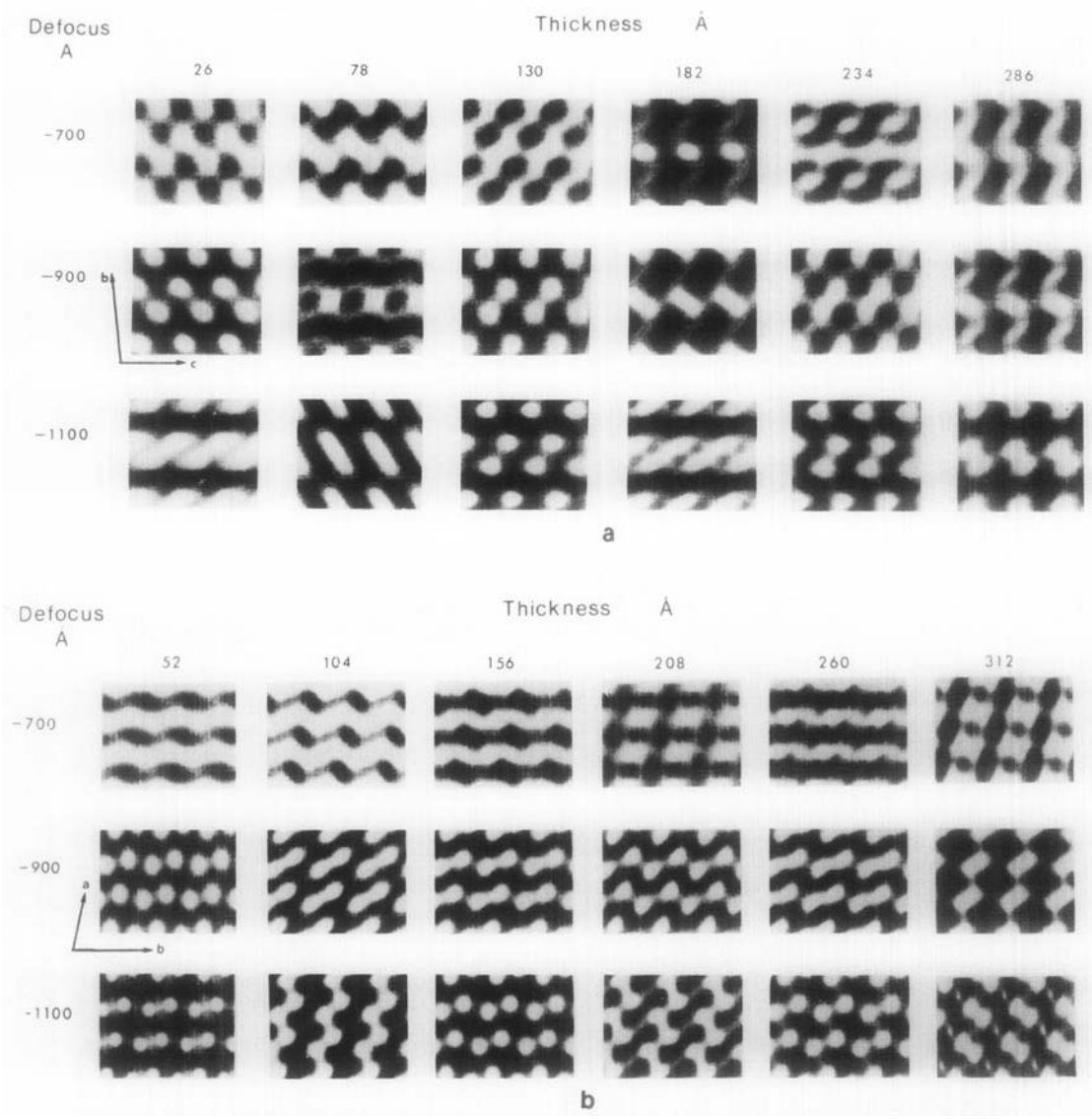

FIG. 4. (a) Calculated $(100)_9$ lattice images of proposed model of ζ phase (Pr_9O_{16}). (b) Calculated $(001)_9$ lattice images of proposed model of ζ phase (Pr_9O_{16}).

also show a periodic occurrence of the thin crystal image at 130–150 and 234–260 Å at defocus values increasing to −1100 Å. At other crystal thicknesses the contrast is modified and no longer corresponds to the projected potential of the structural model. The projection of the unit cell, however, can be seen for any thickness calculated at any value of defocus. This is of great importance in the unambiguous identification of any phase in crystals of uncertain thickness.

Figure 5 is an experimental electron microscope image of ζ phase taken with the electron beam parallel with the ⟨001⟩ axis of the supercell at −900 Å defocus. The dark contrast near the edge of the crystal (bottom of photograph) is due to the first equal-thickness contour. At least three higher

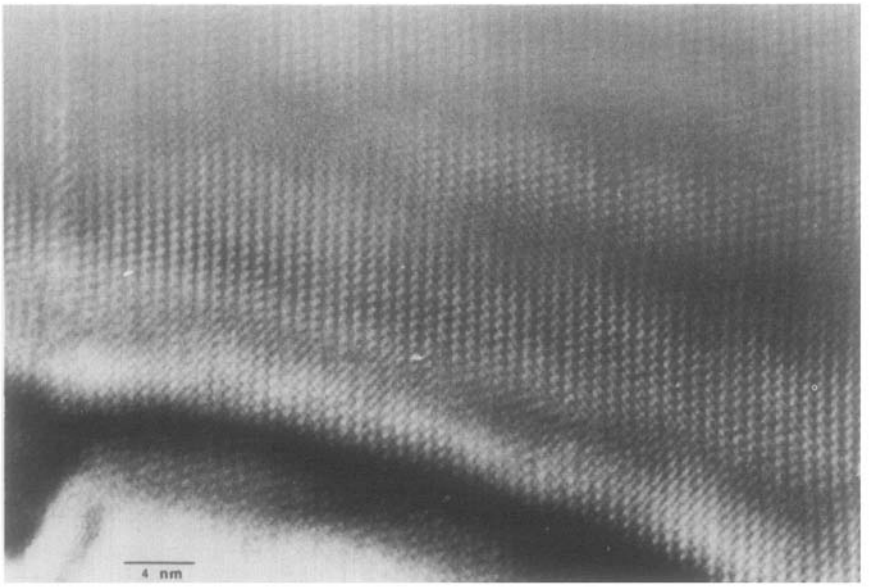

FIG. 5. An experimental electron microscope image of ζ phase taken with the electron beam parallel to the $\langle 001 \rangle$ axis of the supercell at a defocus of −900 Å.

equal-thickness contours can be seen in this image, indicating that it is not of sharp wedge form, characteristic of the crystalline fragments of the rare earth oxides. The contrast in the thin region outside the first contour is neither sharp nor regular. The image generally diplays one white spot per unit cell as is calculated for thicknesses of 300 Å and greater. The narrow region between the first and third equal-thickness contours shows two white spots per cell with an arrangement similar to that in one of the calculated images shown in Fig. 4b (thickness 104 Å and −900 to −1100 Å defocus). No reasonable correspondence could be made with the crystal structure images calculated from the other vacancy model (Fig. 1b).

An experimental image of a crystal of ζ obtained with the electron beam parallel to the $\langle 100 \rangle_9$ axis at a defocus of −900 Å is reproduced in Fig. 6. Generally, the contrast consists of two resolved white spots per unit cell in the same arrangement as that of the projected vacancies in the structural model proposed by Kunzmann and Eyring (Fig. 1a). Since this image was not obtained outside the first equal-thickness contour, it probably corresponds to a thickness of 130 or even 234 Å, where the thin crystal image repeats (Fig. 4b). The inset, a $\langle 100 \rangle_9$ image calculated at a thickness of 130 and −900 Å underfocus, shows the similarity. Again, for this zone, the images calculated from the alternate vacancy model did not exhibit any similarity to the experimental image.

ε Phase—$Pr_{40}O_{72}$

A number of crystals of the ε phase of $Pr_{40}O_{72}$ were examined by single-crystal X-ray diffraction (*5*). Crystals obtained from different preparations displayed various degrees of sharpness of both superlattice and sublattice reflections observed on Laue photographs, some crystals producing diffuse spots and others extremely sharp ones. Refined autodiffractometer settings gave the lattice parameters $a = 6.728(4)$ Å, $b = 19.319(12)$ Å, $c = 15.480(10)$ Å, and $\beta = 125.46(4)°$ which conform to the choice of unit cell obtained from electron diffraction

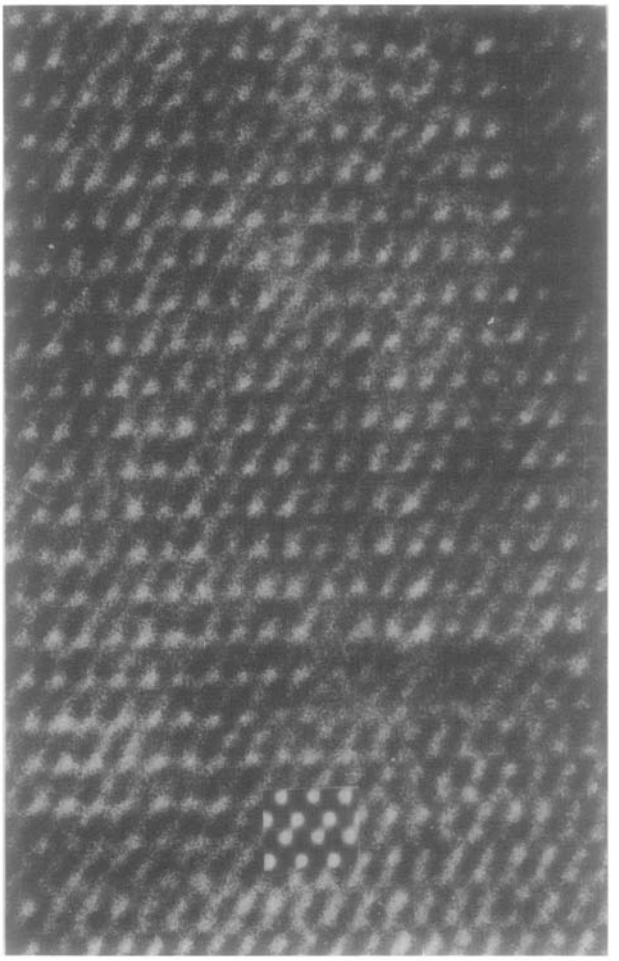

FIG. 6. An experimental image of ζ phase in the $\langle 100 \rangle_9$ zone at a defocus of -900 Å. The inset is the calculated image.

photographs (*4*). A more convenient monoclinic cell with $a = 6.728$ Å, $b = 19.319$ Å, $c = 12.800$ Å, and $\beta = 100.19°$ was later chosen having axial relationships to the fluorite structure given by:

$$a = \tfrac{1}{2}a_F - \tfrac{1}{2}b_F + c_F,$$

$$b = \tfrac{5}{2}(b_F + c_F),$$

$$c = \tfrac{3}{2}a_F + \tfrac{3}{2}b_F + c_F.$$

The pattern of extinctions observed on precession photographs and also from diffractometer data appeared to be $h0l$, $l = 2n+1$ and $0k0$, $k = 2n+1$ which conforms to the space group $P2_1/c$. This was further confirmed by an $N(z)$ test (*13*) on the diffractometer data for the superlattice reflections which indicated a centrosymmetric intensity distribution.

A set of idealized coordinates based on the fluorite substructure was developed for the second choice of unit cell in the space group $P2_1/c$. The unit-cell contents of such a set of sites is $Pr_{40}O_{80}$; hence two of the unique oxygen positions must be vacant to give the ϵ phase composition, $Pr_{40}O_{72}$. The symmetry constraints imposed by the $P2_1/c$ space group in addition to the restriction that two

TABLE II

POSSIBLE VACANCY POSITIONS FOR ε PHASE

Model	Atom	Ideal vacancy position		
		x	y	z
1	O1	0.0625	0	0.1875
	O14	0.1875	0.3	0.0625
2	O1	0.0625	0	0.1875
	O15	0.3125	0.3	0.4375
3	O1	0.0625	0	0.1875
	O16	0.4375	0.2	0.3125
4	O5	0.0625	0.4	0.1875
	O16	0.4375	0.2	0.3125
5	O9	0.5625	0.1	0.1875
	O10	0.6875	0.4	0.0625
6	O9	0.5625	0.1	0.1875
	O14	0.1875	0.3	0.0625
7	O11	0.8125	0.4	0.4375
	O14	0.1875	0.3	0.0625
8	O11	0.8125	0.4	0.4375
	O16	0.4375	0.2	0.3125

oxygen vacancies cannot lie on adjacent sites result in eight unique and chemically plausible models for the structure of this phase. These vacancy models are presented in Table II.

Crystal structure images were calculated for the $\langle 100\rangle_{10} = \langle 21\bar{1}\rangle_F$ zone for all of the eight possible vacancy models of ε phase via the multislice method as described previously. In each case the four metal atoms surrounding each vacancy were displaced about 0.17 Å away from the vacancy to conform with the results of the neutron diffraction study of Pr_7O_{12} (*2*). The oxygen atoms were retained on the ideal fluorite positions.

A relatively low-magnification electron microscope image of ε obtained with the electron beam aligned parallel to the a-axis of the monoclinic superstructure ($\langle 21\bar{1}\rangle_F$ zone) is shown in Fig. 7. This image was

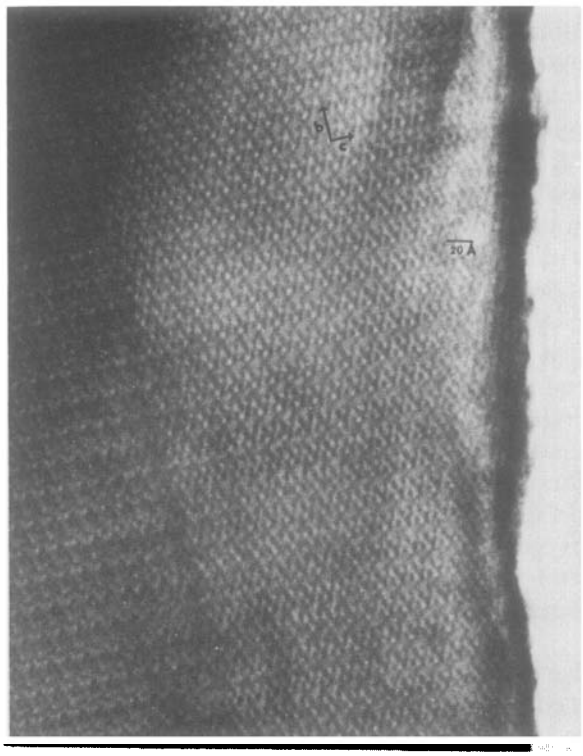

FIG. 7. Observed crystal structure image from a $\langle 100\rangle_{10}$ zone of ε phase ($Pr_{10}O_{18}$).

recorded from a relatively thin crystalline fragment at a defocus of approximately −900 Å. The first equal-thickness contour which occurs at about 70 Å for this phase is right at the edge of this crystal and thus is not of the thin wedge shape desired for high-resolution imaging. The abrupt change in contrast approximately two-thirds of the distance in from the edge is probably due to a step. Between the edge and the step a rectangular array of bright spots about 13 × 20 Å corresponding to the projection of the monoclinic cell along the a-axis can be seen. During the electron microscope observation of ε phase the electron beam was maintained as low as possible in order to minimize structural changes caused by the interaction of the electron beam with the specimen. This phase is less stable in the beam at the residual atmosphere in the column than ζ phase.

In Fig. 8 an electron micrograph of another thin crystal of $Pr_{40}O_{72}$ is displayed at a higher magnification. This image, which was obtained at −900 Å defocus with the electron beam oriented parallel with the a-axis, consists of eight white spots per unit cell. The arrangement of the white spots corresponds quite well to the positions of the oxygen vacancies in vacancy model 4 (Table II) for the structure of the $n = 10$ member of the homologous series which is drawn in projection in Fig. 9. The filled circles, squares, and triangles represent 8-, 7-, and 6-coordinated metal atoms, respectively, and the open circles represent oxygen vacancies. The relaxed metal and ideal oxygen positions for vacancy model 4 are given in Table III. In this vacancy model all of the vacant oxygen positions occur pairwise across metal atoms creating four octahedrally coordinated metal atoms per cell.

Dynamically calculated electron microscope images obtained from oxygen vacancy model 4 for ε phase are shown as a function of defocus value and crystal thickness in Fig. 10. These $\langle 100\rangle_{10} = \langle 21\bar{1}\rangle_F$ images each display twice the unit-cell repeat in the b- and c-directions. They were calculated using 1500 beams for an objective aperture of radius 0.285 $Å^{-1}$ (59 beams in the aperture) and a beam divergence angle of 0.9 mrad. The thin crystal (26 Å) image at −900 Å defocus represents the projected crystal structure of ε phase as seen by comparison with Fig. 9 and agrees very well with the experimental image in Fig. 8. Also, this structure image repeats with thickness at 135 and 270 Å, analogous to the repeating of the images calculated for ζ phase. Calculated images based on the other seven plausible vacancy models for ε did not exhibit contrast resembling that in the observed images.

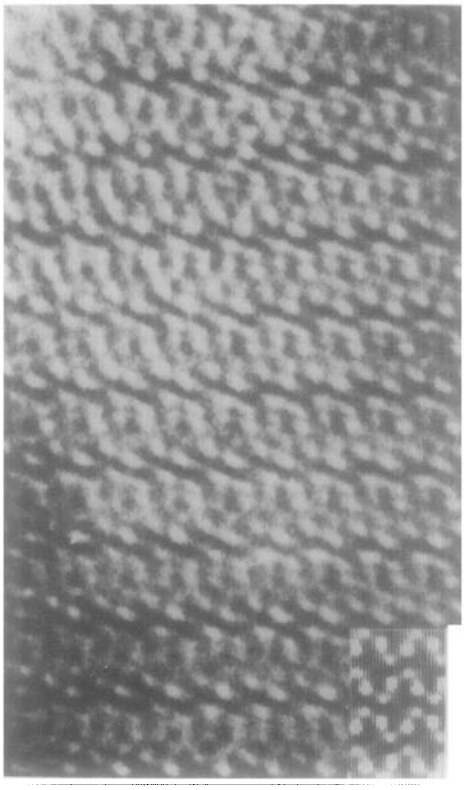

FIG. 8. Observed and calculated lattice images from a $\langle 100\rangle_{10} = \langle 21\bar{1}\rangle_F$ zone of $Pr_{19}O_{18}$ showing vacancy arrangement.

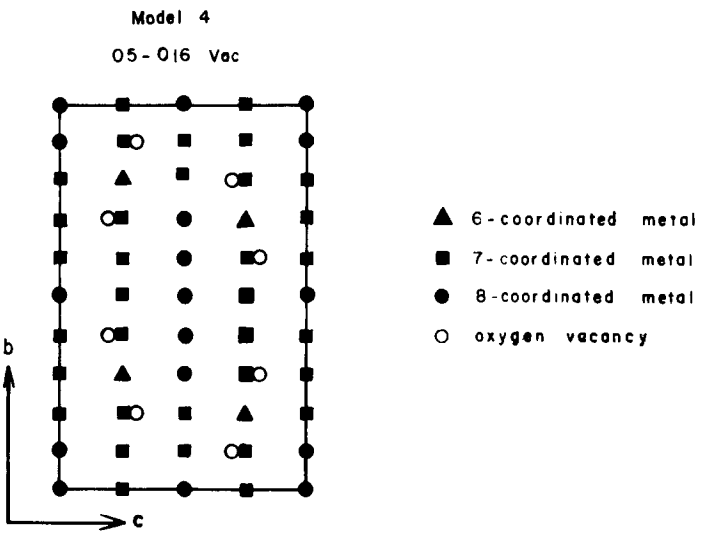

FIG. 9. A projection of the proposed structure of ε phase along the $\langle 100 \rangle_{10}$ zone.

In the proposed structural model for $Pr_{40}O_{72}$ shown in Fig. 9 all of the oxygen vacancies occur pairwise across a body diagonal of an MO_8 cube as they do in the refined structure of Pr_7O_{12} and the proposed structure of Pr_9O_{16}. Also, the arrangement of the vacancy doublets in the a-axis direction ($\frac{1}{2}[21\bar{1}]_F$) is the same in ε phase as in the other members of the homologous series of rare earth oxides. The proposed model for the structure of $Pr_{40}O_{72}$ has octahedrally coordinated metal atoms at $\frac{1}{4}, \frac{1}{5}, \frac{3}{4}$; $\frac{1}{4}, \frac{3}{10}, \frac{1}{4}$; $\frac{3}{4}, \frac{7}{10}, \frac{3}{4}$; and $\frac{3}{4}, \frac{7}{10}, \frac{3}{4}$. The vector between the first and second pairs of positions is a $\frac{1}{2}[211]$

TABLE III

ATOM POSITIONS FOR VACANCY MODEL 4 OF ε PHASE SYMMETRY $P2_1/c$

Atom	x	y	z	Atom	x	y	z
Pr1	0	0	0	O1	0.0625	0	0.1875
Pr2	0.5	0	0.5	O2	0.1875	0.5	0.0625
Pr3	0.25995	0.51059	0.25020	O3	0.3125	0.5	0.4375
Pr4	−0.01538	0.40233	−0.01070	O4	0.4375	0	0.3125
Pr5	0	0.3	0.5	O6	0.1875	0.1	0.0625
Pr6	0.51538	0.19767	0.50170	O7	0.3125	0.1	0.4375
Pr7	0.5	0.1	0	O8	0.4375	0.4	0.3125
Pr8	0.24005	0.08941	0.24980	O9	0.5625	0.1	0.1875
Pr9	0.25	0.3	0.25	O10	0.6875	0.4	0.0625
Pr10	0.72332	0.40420	0.25488	O11	0.8125	0.4	0.4375
Pr11	0.77668	0.19580	0.24512	O12	0.9375	0.1	0.3125
				O13	0.0625	0.2	0.1875
				O14	0.1875	0.3	0.0625
Vacancy				O15	0.3125	0.3	0.4375
				O17	0.5625	0.3	0.1875
1.	0.0625	0.4	0.1875	O18	0.6875	0.2	0.0625
2.	0.4375	0.2	0.3125	O19	0.8125	0.2	0.4375
				O20	0.9375	0.3	0.3125

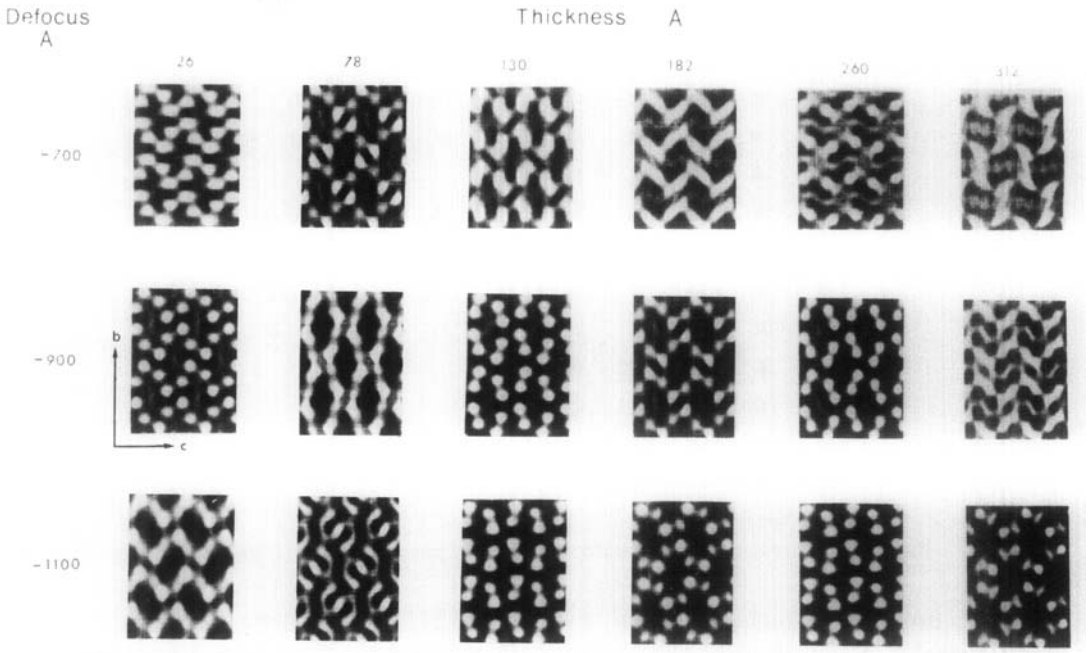

FIG. 10. Calculated electron microscope images for the model illustrated in Fig. 9 as a function of thickness and defect of focus.

vector. Furthermore, if the oxygen vacancy pair near the metal atoms at $\frac{3}{4}, \frac{4}{5}, \frac{1}{4}$ and $\frac{1}{4}, \frac{1}{5}, \frac{3}{4}$ were rotated by 180° about an axis parallel to the b-axis, the unit cell will be one-fourth the volume of the observed cell and the subunit would in fact be the primitive triclinic cell for the $n = 10$ member of the series described by Kunzmann and Eyring (*4*). The observed monoclinic cell can be described in terms of a chemical twinning about two perpendicular planes; first about a $(\bar{1}11)_F$ plane, then about a $(110)_F$ plane.

The structural model proposed by Kunzmann and Eyring (*4*) for the odd members of the homologous series consists of octahedrally coordinated metal atoms all lying on $(135)_F$ planes with every nth [where n is the subscript in the formula (R_nO_{2n-2})] containing the octahedral metal atoms. The same structural principle seems to apply to the even members as suggested for the proposed model of β phase ($Pr_{24}O_{44}$) (*3*) in which case the 6-coordinated metal atoms all occur on alternate segments of $(135)_F$ and $(1\bar{5}\bar{3})_F$ planes. The proposed structure for $Pr_{40}O_{72}$ is consistent with this principle although the oxygen vacancy pairs across the octahedrally coordinated metal atoms are alternately rotated by 180°.

The δ Phase Polymorph—$PrO_{1.818}$

Crystalline fragments of the δ-phase polymorph ($PrO_{1.818}$) were found together with crystals of $Pr_{40}O_{72}$ and $Pr_{24}O_{44}$. Crystals sufficiently large for X-ray diffraction studies were not obtained. This $n = 11$ member of the homologous series of intermediate phases in the praseodymium oxide system has not been prepared as a single phase although its existence was indicated from tensimetric (*14*) and high-temperature powder X-ray studies (*15*).

An electron diffraction pattern obtained with the electron beam aligned parallel to the a-axis of this superstructure, which is common with that of the other members of the series, is shown in Fig. 11. The unit cell of this phase is monoclinic and can be described by

the cell constants $a = 6.7$ Å, $b = 42.5$ Å, $c = 15.5$ Å, and $\beta = 125.2°$ having axial relationships to the fluorite substructure given by:

$$a = a_F + \tfrac{1}{2}b_F - \tfrac{1}{2}c_F,$$
$$b = \tfrac{11}{2}(-b_F - c_F),$$
$$c = 2(-b_F - c_F).$$

The content of this monoclinic unit cell is $Pr_{88}O_{160}$, including 16 oxygen vacancies per cell. The cell volume is eight times that of the primitive triclinic cell described by Kunzmann and Eyring for the $n = 11$ member of the homologous series. The primitive triclinic unit referred to as δ phase is well known in the terbium oxide system but has not been observed in the praseodymium

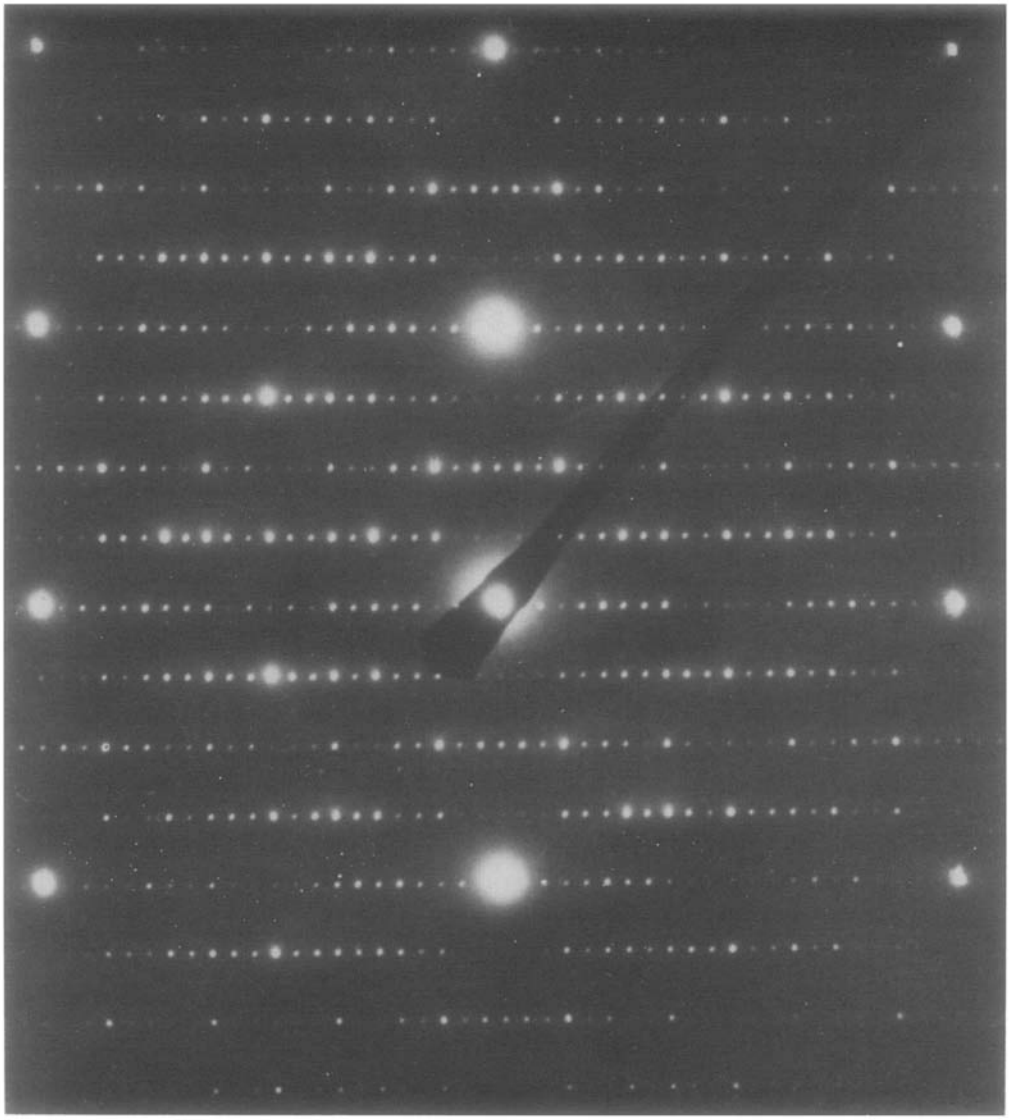

FIG. 11. An electron diffraction pattern with the electron beam along the a-axis of the δ (2) Phase $Pr_{88}O_{160}$.

oxides. The larger monoclinic polymorph which will hereafter be referred to as the δ (2) phase has not been observed in the terbium oxides.

This δ-phase polymorph is very unstable in the electron beam of the microscope, readily disordering and also decomposing into ε and β phases. Even with extremely low illumination during electron microscope imaging some disordering was observed to occur. Some high-resolution images, however, were obtained as shown in Fig. 12. This image was obtained with the electron beam oriented parallel to the a-axis of δ (2) with about -900 Å defocus. The projection of the monoclinic unit cell is delineated. The contrast is not uniform across the micrograph, probably due to disordering in the electron beam. This image cannot be interpreted intuitively in structural terms, and a comparison of the image contrast with that resulting from possible oxygen vacancy models was not attempted due to the size and complexity of this superstructure.

It is not unlikely, however, in view of the relationship of the lattice vectors of the δ (2) phase to those of the other members in the homologous series of praseodymium oxides, that the structural principle involving vacancy doublets may extend to this low-stability homolog.

Conclusion

The most successful method of elucidating the structures of the fluorite-related intermediate oxides of praseodymium has been HRTEM. Significant advances have been outlined here toward an understanding of the structural principle relating members of the homologous series where the traditional methods of X-ray and neutron diffraction on available specimens have not been successful. This is particularly significant since these

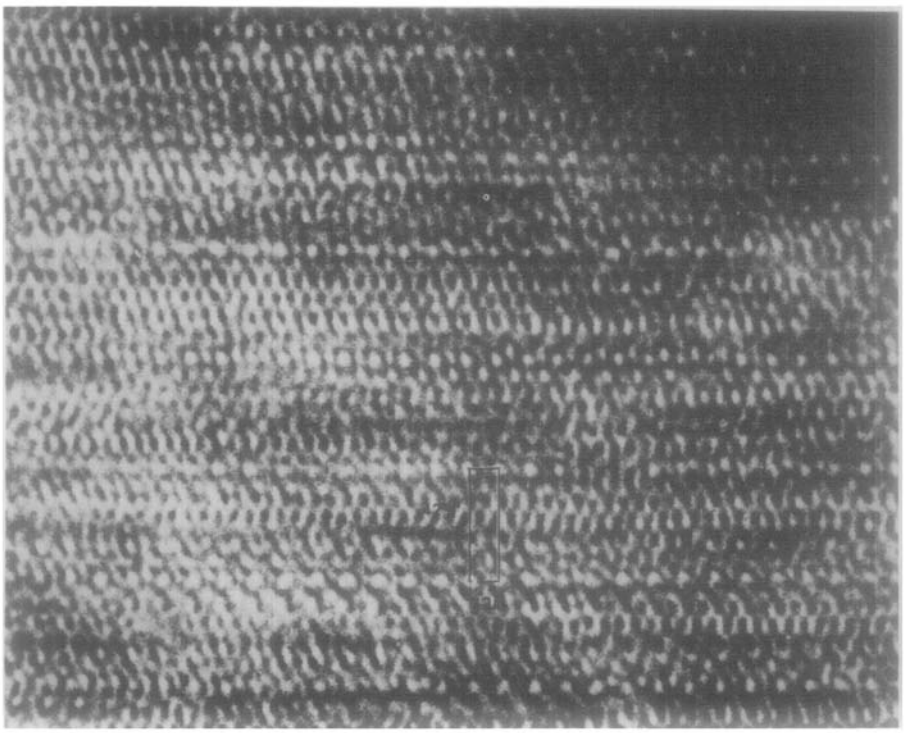

FIG. 12. Observed image from a $(100)_{11}$ zone of the δ (2) phase $Pr_{88}O_{160}$.

ubiquitous fluorite-related materials are not particularly well suited to HRTEM, suggesting that most thermally stable materials can be studied by this means.

Acknowledgments

We wish to thank Mike McKelvy and Sung Pack for assistance in crystal growth and compositional adjustment. Also, it is a pleasure to thank the Arizona State University Computer Center and the CSSS Electron Microscope Laboratory and its manager, John Wheatley, for the use of their facilities.

References

1. A. J. SKARNULIS, E. SUMMERVILLE, AND L. EYRING, *J. Solid State Chem.* **23**, 59 (1978).
2. R. B. VON DREELE, L. EYRING, A. L. BOWMAN, AND J. L. YARNELL, *Acta Crystallogr. Sect. B* **31**, 971 (1975).
3. E. SUMMERVILLE, R. T. TUENGE, AND L. EYRING, *J. Solid State Chem.* **24**, 21–31 (1978).
4. P. KUNZMANN AND L. EYRING, *J. Solid State Chem.* **14**, 229 (1975).
5. R. B. VON DREELE, unpublished results.
6. M. Z. LOWENSTEIN, L. KIHLBORG, K. H. LAU, J. M. HASCHKE, AND L. EYRING, *Nat. Bur. Stand. USA Spec. Publ.* **364**, 343 (1972).
7. S. IIJIMA, *Acta Crystallogr. Sect. A* **29**, 18 (1973).
8. J. G. ALLPRESS, E. A. HEWAT, A. F. MOODIE, AND J. V. SANDERS, *Acta Crystallogr. Sect. A* **28**, 528 (1972).
9. M. A. O'KEEFE, *Acta Crystallogr. Sect. A* **29**, 389 (1973).
10. J. M. COWLEY AND A. F. MOODIE, *Acta Crystallogr. Sect. A* **10**, 609 (1957).
11. "International Tables for X-Ray Crystallography," Vol. 4, p. 99, Table 2.2B, Kynoch Press, Birmingham (1974).
12. E. SUMMERVILLE, private communication.
13. E. R. HOWELLS, D. C. PHILLIPS, AND D. ROGERS, *Acta Crystallogr.* **3**, 210 (1950).
14. B. G. HYDE, D. J. M. BEVAN, AND L. EYRING, *Phil. Trans. Roy. Soc. London Ser. A* **259**, No. 1106, 583–614 (1966).
15. R. P. TURCOTTE, M. S. JENKINS, AND L. EYRING, *J. Solid State Chem.* **7**, 454–460 (1973).